Materials Science & Engineering A 701 (2017) 56–68

Contents lists available at ScienceDirect

Materials Science & Engineering A

journal homepage: www.elsevier.com/locate/msea

Homogenization and texture development in rapidly solidified AZ91E consolidated by Shear Assisted Processing and Extrusion (ShAPE)

N.R. Overman[a,*], S.A. Whalen[a], M.E. Bowden[a,b], M.J. Olszta[a], K. Kruska[a], T. Clark[c], E.L. Stevens[d], J.T. Darsell[a], V.V. Joshi[a], X. Jiang[a], K.F. Mattlin[a], S.N. Mathaudhu[a,c]

[a] Pacific Northwest National Laboratory, P.O. Box 999, Richland, WA 99352, United States
[b] Environmental Molecular Sciences Laboratory (EMSL), 3335 Innovation Blvd., Richland, WA 99354, United States
[c] University of California, Riverside, 3401 Watkins Dr., Riverside, CA 92521, United States
[d] University of Pittsburgh, 4200 5th Avenue, Pittsburgh, PA 15260, United States

ARTICLE INFO

Keywords:
Rapid solidification
Magnesium alloy
Microstructure
ShAPE
Friction consolidation extrusion
EBSD

ABSTRACT

Shear Assisted Processing and Extrusion (ShAPE) -a novel processing route that combines high shear and extrusion conditions- was evaluated as a processing method to densify melt spun magnesium alloy (AZ91E) flake materials. This study illustrates the microstructural regimes and transitions in crystallographic texture that occur as a result of applying simultaneous linear and rotational shear during extrusion. Characterization of the flake precursor and extruded tube was performed using scanning and transmission electron microscopy, x-ray diffraction and microindentation techniques. Results show a unique transition in the orientation of basal texture development. Despite the high temperatures involved during processing, uniform grain refinement and material homogenization are observed. These results forecast the ability to implement the ShAPE processing approach for a broader range of materials with novel microstructures and high performance.

1. Introduction

Traditionally, alloying magnesium with other lightweight structural materials such as aluminum or zinc has served two key purposes: 1) improving the corrosion resistance by lowering base metal reactivity of Mg and 2) enhancing microstructural refinement, reducing grain size and improving the mechanical properties [1,2]. Improvements in both the corrosion resistance and strength-to-weight ratios have elevated market demand in the automotive and aircraft industries where these property enhancements translate to reduced material cost and improved fuel efficiency [3–7].

The past two to three decades of research on these materials has focused heavily on the design of key alloy chemistries and heat treatments to optimize application-specific properties [8–13]. Much of the work performed on these alloy systems has focused on conventional production techniques, mechanical processing and post-fabrication heat treatments. The ultimate tensile strengths of AZ91, the most popular commercially available magnesium casting alloy, can be nearly doubled from 172 MPa in the as-cast condition to 342 MPa following extrusion and a T6 temper [10,14]. This heat-treatable, die/sand casting alloy was developed for general purpose, structural applications [15] due to its excellent corrosion resistance, high tensile strength and moderate yield strength.

The primary mechanisms responsible for strength increases in AZ91 are precipitation strengthening; primarily via formation of the $Mg_{17}Al_{12}$ phase- and grain refinement [16–18]. The contribution of precipitation strengthening in this alloy, however is relatively small when compared with precipitation hardened Al-alloys. The decreased strengthening effect has been attributed to precipitate orientation with respect to the primary slip mode (basal slip), wherein precipitates are either thin platelets on the basal plane or narrow rods along the c-axis perpendicular to the basal plane; neither effectively hinders basal slip [18]. Based on these observations, it appears that an effective way to increase the strength of AZ91 would be to develop a processing methodology that could increase the number density of blocky/spherical precipitates and redistribute them within the matrix. Ideally, the grain size would remain small and a high fraction of second phase precipitates would pin grain boundary and dislocation movement and promote strength increases. Precipitation of equilibrium $Mg_{17}Al_{12}$ intermetallics along grain boundaries would also need to be suppressed as this has been shown in the literature to form a divorced eutectic leading to brittle boundary interfaces and increased creep susceptibility at elevated temperatures [19,20]. Processing methodologies that promote metastable, non-equilibrium states, such as rapid solidification (RS) offer potential improvements in the strength of AZ91 through extension of

* Corresponding author.
E-mail address: Nicole.Overman@pnnl.gov (N.R. Overman).

http://dx.doi.org/10.1016/j.msea.2017.06.062
Received 17 December 2016; Received in revised form 6 June 2017; Accepted 14 June 2017
Available online 19 June 2017
0921-5093/

Table 1
Alloy composition as measured by ICP-OES (in wt%).

Alloy	Mg	Al	Zn	Mn
AZ91E	89	6.4	0.5	0.22

Trace ($\leq$0.01 wt%) Cu, Ni, Fe, Si, P, Li

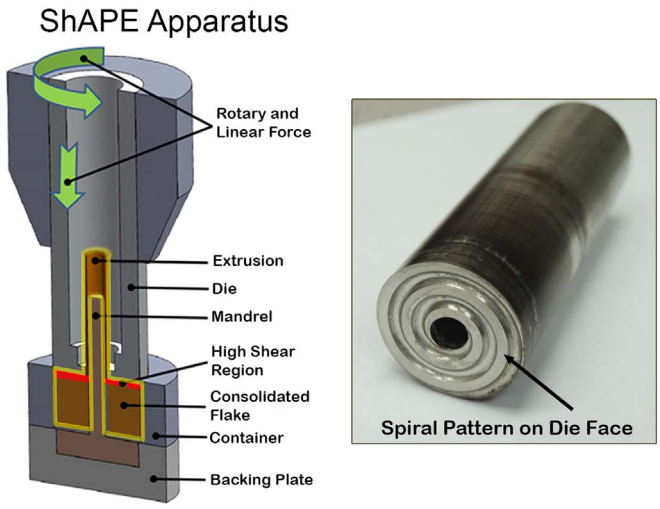

Fig. 1. Processing diagram showing indirect extrusion with the high shear region highlighted in red, the consolidated flake (housed in the container) and extruded tube highlighted in yellow. An image of the die (right) illustrates the spiral scroll pattern on the surface that contacts the high shear region during processing. (For interpretation of the references to color in this figure legend, the reader is referred to the web version of this article.)

Table 2
ShAPE process parameters.

Material	Flake Quantity (g)	Pre-Load (MPa)	Tool Speed (rpm)	Plunge Rate (mm/min)	Extrusion Ratio (A_{flake}/A_{tube})
AZ91E Flake	15	56.6	500	3.8	46.8

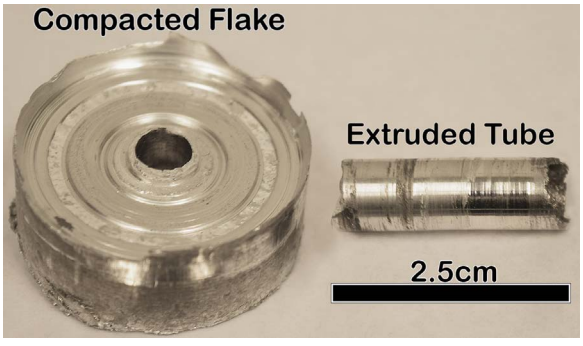

Fig. 2. Compacted flake and extruded tube formed during processing. The left side of the tube is the location where it was separated from the compacted flake material.

solid solubility limits [21–23] and ultimately formation of finely dispersed secondary phases [24].

Melt spinning is an RS approach that has demonstrated novel metastable microstructural states. In this approach, metal is heated above an internally water-cooled copper wheel, and when fully melted, it is ejected through an orifice onto the wheel. As the fine stream of liquid metal impinges on the spinning wheel it solidifies at very high cooling rates (greater than 10^4 K/s) [25]. Amorphous, nano-crystalline and quasi-crystalline microstructures are a common result of melt spinning RS processing and can contribute to mechanical properties due to

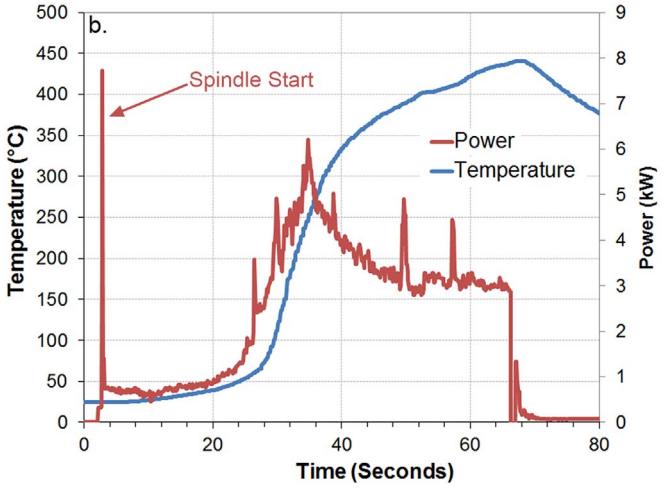

Fig. 3. Die face temperature and spindle power as a function of process time.

microstructural refinement, supersaturated solid solution, refined grain size strengthening and an increased number density of fine precipitates [26,27].

Conversion of novel flake or particulate materials into bulk, full-density products can prove to be challenging as the temperature necessary often results in the loss of the beneficial metastable microstructures, thus novel approaches that facilitate retention of unique microstructural states are in need of exploration [28,29]. The Shear Assisted Processing and Extrusion (ShAPE) technique utilizes a rotating die as opposed to the axially fed die used in the conventional indirect extrusion process [30]. When the rotating ram face comes in contact with the particulate or flake material, it is compacted and densified as the forging load is applied. The combined action of the forging load with the rotating die face forces the underlying material to undergo severe plastic deformation without melting, and allows it to flow plastically through an extrusion orifice. The addition of scroll features on the ram face aid in material flow toward the extrusion orifice [30,31] as it is indirectly extruded. Friction stir back extrusion of aluminum alloy AA7277 machining chips has also shown the importance of scrolled features on the die face [32,33]. Analogous techniques utilizing friction extrusion of solid Mg and Al alloy billets are found in the literature [34–37] but are significantly different from the ShAPE process utilized in this work due to the simultaneous linear and rotation shear applied during extrusion.

In this study we seek to investigate the microstructural evolution of AZ91E rapidly solidified precursor material as it is processed into an indirect extrusion tube using the ShAPE process. It is hypothesized that the high-shear, lower-temperature thermomechanical conditions inherent to the ShAPE process will enable the retention of metastable microstructures present in the precursor flakes, and concomitantly, novel textures not possible through conventional extrusion routes.

2. Material and methods

2.1. Melt spinning

The AZ91E material used in this study was provided by U.S. Magnesium LLC (Salt Lake City, Utah, USA). The starting ingot material was machined into ~150 g sections that were placed into a boron nitride coated graphite crucible and melt processed in a 300 g batch. The melt spinning chamber was placed under vacuum and purged with argon three times to ensure maximum oxygen removal from the flake chamber. Prior to heating, the crucible was backfilled with a mixture of CO_2 and SF_6 gas to prevent oxidation of the molten magnesium. Temperature was monitored above the melt in the crucible, and the internal temperature of the melt was also periodically evaluated to

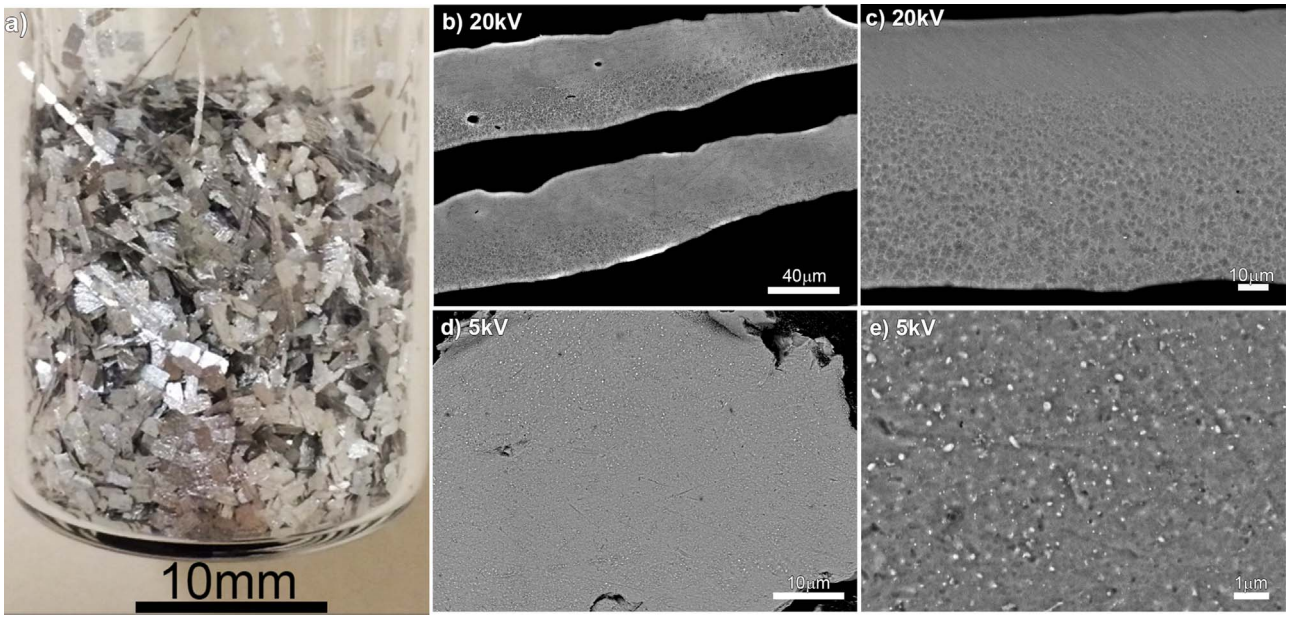

Fig. 4. As produced AZ91E rapidly solidified flake material is shown in (a) along with a cross sectional views obtained using 20 kV SEM backscatter imaging conditions (b, c) as well as 5 kV SEM backscatter imaging (d, e) that illustrate formation of second phases.

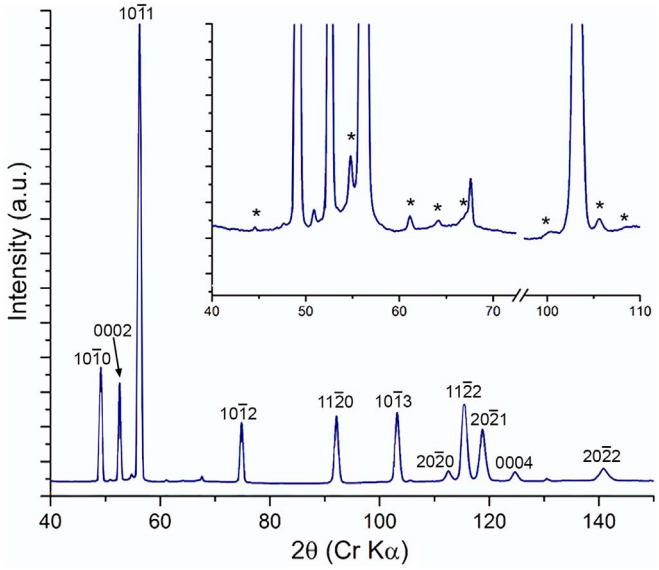

Fig. 5. XRD measurements performed on the as fabricated AZ91 flake material indicate the majority of the surface was found to be α-Mg, as indicated by the overlaid Miller-Bravais indices. Minor $Mg_{17}Al_{12}$ peaks were also observed as indicated by the asterisk markings.

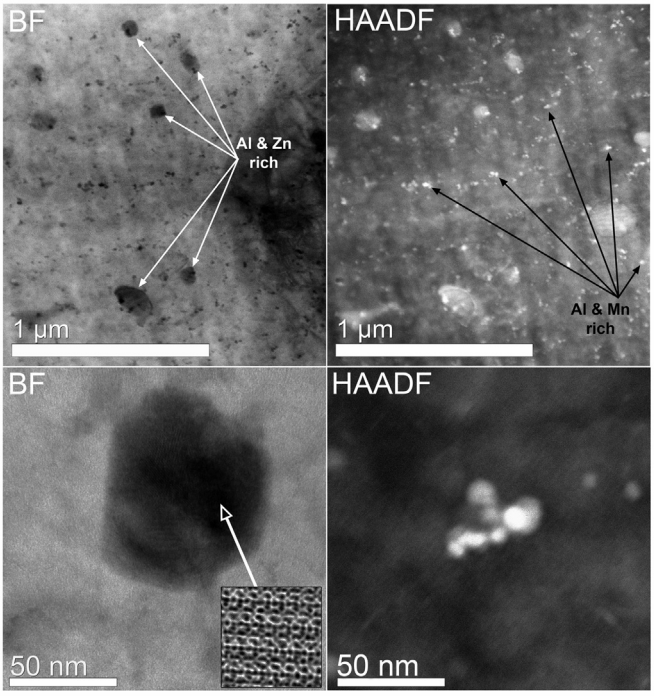

Fig. 6. TEM images of the rapidly solidified flake illustrating precipitate distributions at low magnification (top row) and higher magnification to compare precipitate size (bottom row). The callout showing the precipitate lattice structure has a side length of 3 nm.

ensure complete melting. The internal temperature prior to melt spinning was measured at ~775 °C. Following complete melting, the material was rapidly solidified using an internally cooled copper wheel with a knurled pattern spun at 40 m/s to produce RS flake. Prior to opening the flake chamber it was evacuated and backfilled to atmospheric conditions. The composition of the flake material was measured by inductively coupled plasma optical emission spectroscopy (ICP-OES) and is shown in Table 1.

2.2. ShAPE technique

The H13 tool steel ShAPE apparatus as shown in Fig. 1 was used to perform indirect extrusion of thin-walled tubing. Melt spun flake material was loaded into a cylindrical container having an inner diameter of 31.8 mm and height of 21.0 mm. The flakes were then compacted with a pre-load to minimize loose flake exiting through the extrusion orifice during the onset of tool rotation.

During processing, the die (with a 7.5 mm diameter orifice) applied pressure to the flake in the container and rotated around a fixed 6.0 mm diameter mandrel. As the die compacted the flake, the flakes are first consolidated, then back extruded as it was forced vertically through the 0.75 mm gap between the die and mandrel resulting in a tubular geometry.

The tool face consisted of a single spiral scroll to promote material flow toward the extrusion orifice. The die contained a 6.4 mm long

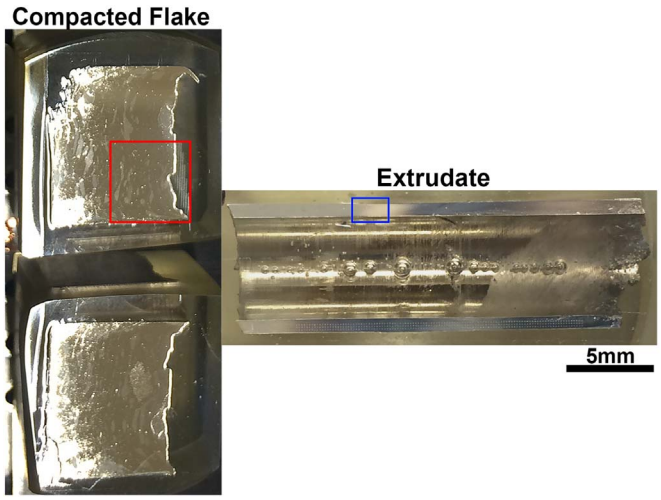

Fig. 7. Polished cross section view of the compacted flake (left) and extrudate (right). The indicated rectangles on the compacted flake (red) and extrudate (blue) correlate with specimen microstructures shown in Fig. 8.

throat and 90° relief to minimize friction between the die wall and extrudate. The resultant tube geometry was nominally 7.5 mm diameter, 25 mm long with a nominal wall thickness of 0.75 mm. Axial force and rotational speed of the die were controlled using an ultra-high precision friction stir welding machine manufactured by Transformation Technologies, Inc. (TTI). Temperature was measured during the process using a type-K thermocouple embedded 1.0 mm behind the die face. The force and rotational speed during extrusion can be adjusted to regulate the applied torque, and consequently the heat generated within the shear material zone. Process parameters are listed in Table 2, the extrusion ratio was calculated by dividing the initial cross sectional areas (A) of the consolidated flake and tube.

One unique aspect of the ShAPE process is that while severe plastic deformation is induced at the die/flake interface, it is simultaneously generated as a result of counter rotation between the die throat and mandrel. This two-step shear process is much different than conventional extrusion techniques and offers the potential for significant grain refinement, distribution and breakdown of second phases, and the ability to potentially impart novel textures.

2.3. Specimen characterization methods

Prior to analysis, all specimens were cold mounted in epoxy and polished to a final surface finish of 0.05 μm. Scanning electron microscopy (SEM) analysis was performed using a JEOL 7600F field emission scanning electron microscope. Electron backscatter diffraction (EBSD) mapping was performed using an accelerating voltage of 20 keV and a working distance of 21 mm. Indexing was accomplished using a magnesium hexagonal crystal structure, Laue group 9, space group 194 and unit cell parameters $a = 3.209$ Å, $b = 3.209$ Å, $c = 5.211$ Å, $\alpha = 90°, \beta = 90°, \gamma = 120°$ which allowed for assessment of the matrix crystal structure at all stages of processing. Only the matrix phase (hexagonal Mg) was indexed during mapping in an effort to reduce analysis duration and cover larger areas to view overall specimen texture. EBSD measurement of highly refined second phases was not performed. Low magnification maps were generated using a 750 nm step size while high magnification mapping was performed using more refined step sizes of 150–250 nm.

Transmission electron microscopy (TEM) specimen preparation was performed using a FEI Quanta 3D Focused Ion Beam (FIB) instrument. TEM analysis (in both transmission and scanning mode (STEM)) was performed at 200 kV with a JEOL ARM 200CF aberration probe corrected microscope, equipped with a high angle Centruio silicon drift detector for x-ray spectroscopy, and a high angle annular dark field (HAADF) detector as well as a STEM bright field detector. Vickers hardness (HV) testing was performed using a fully automated Clark CM-

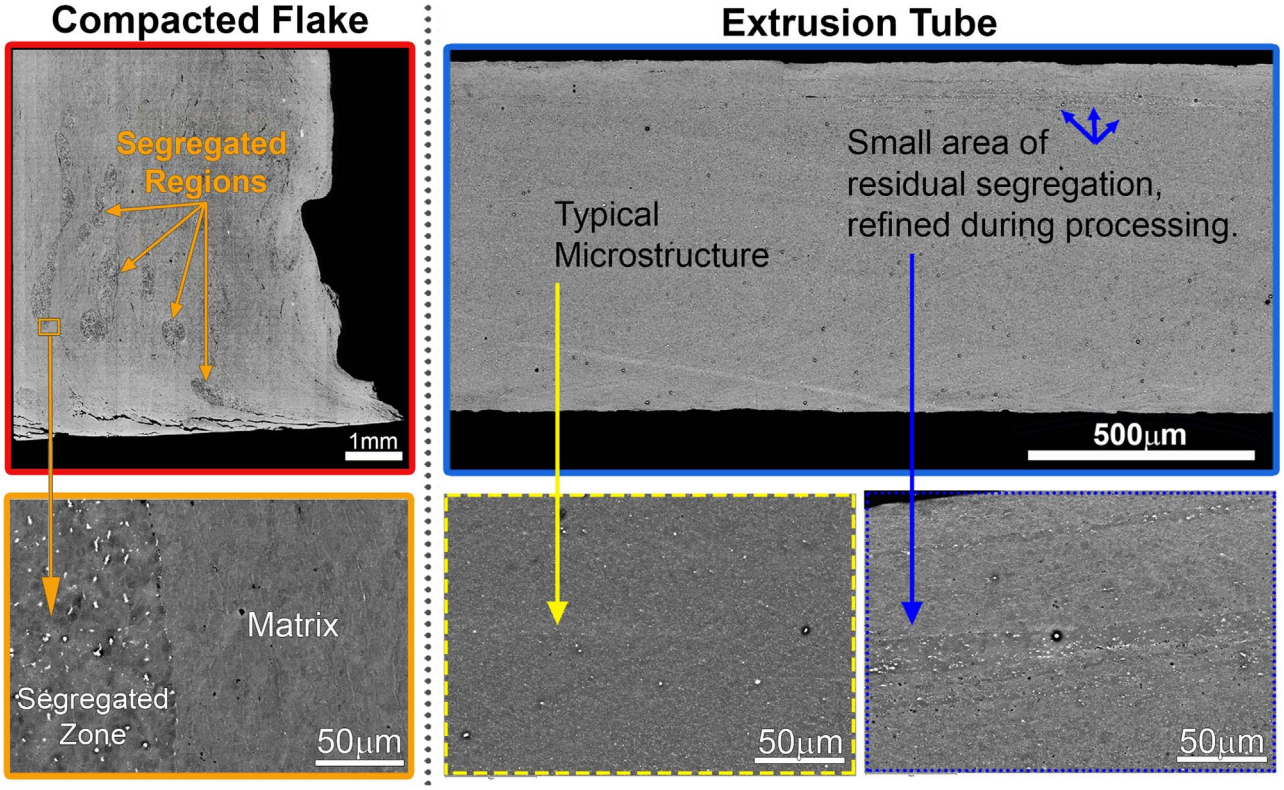

Fig. 8. SEM backscatter montages (top row) depicting cross sections of the compacted flake (left) and extrudate (right). Higher magnification images (bottom row) illustrate precipitate redistribution and material homogenization within the extrudate.

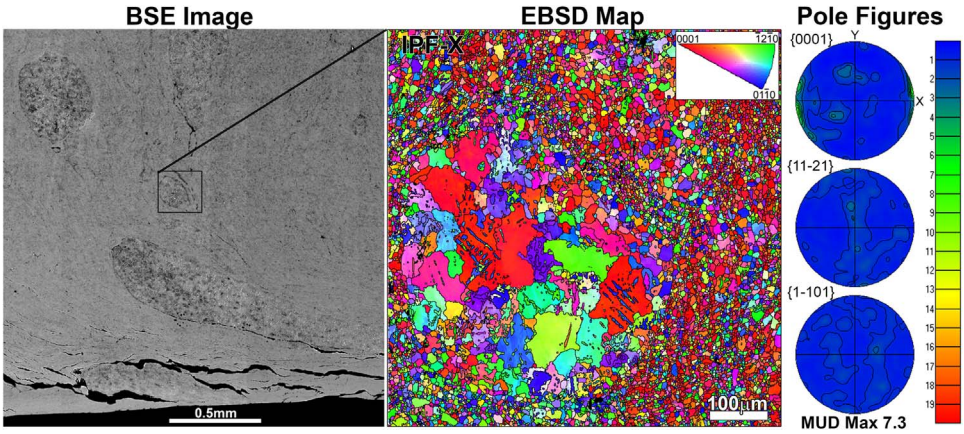

Fig. 9. EBSD from a segregated region within the compacted flake showing localized grain growth.

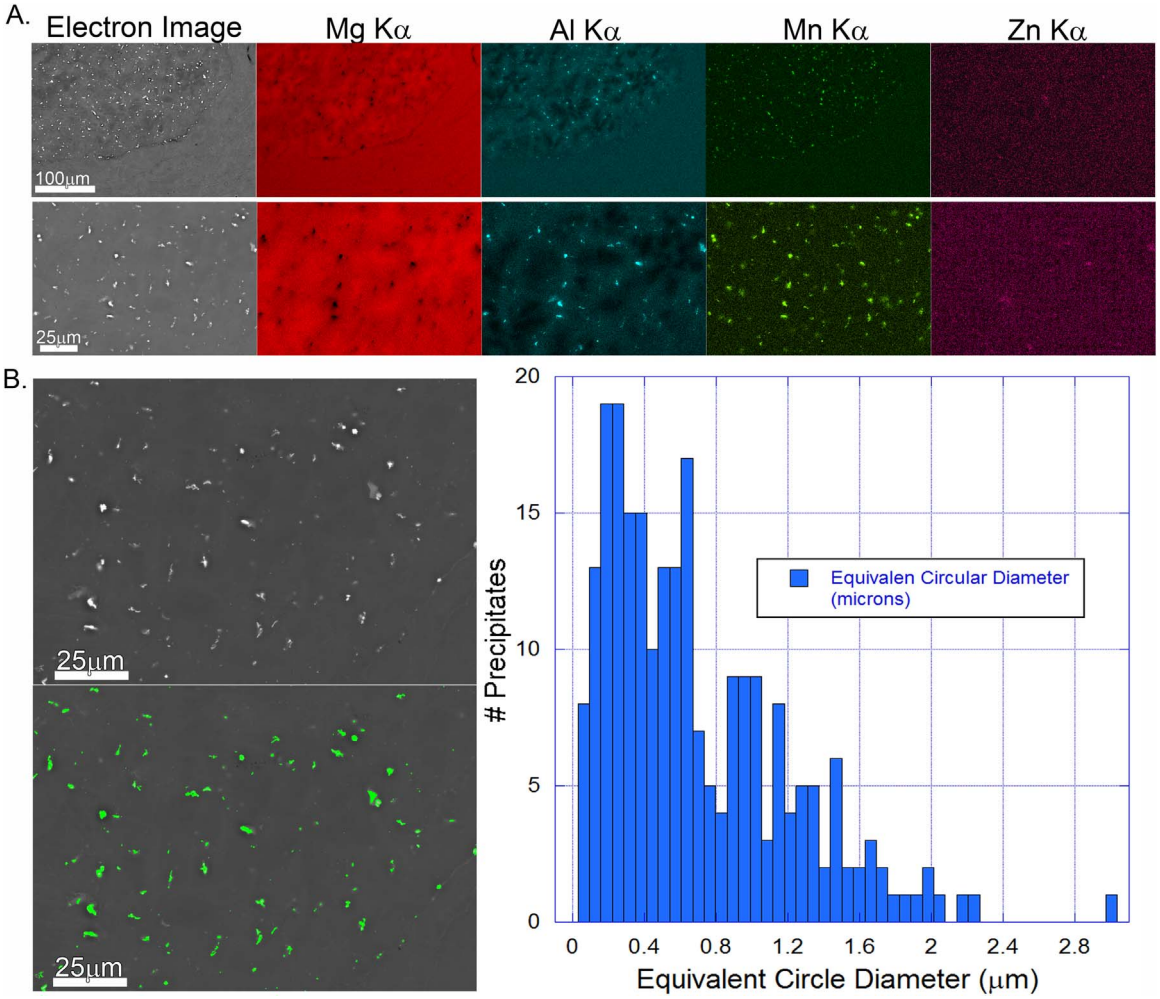

Fig. 10. A) EDS maps at two different magnifications were generated from a segregated region of the compacted flake showing Al + Mn precipitates in addition to Al + Zn precipitates. B) Threshold adjusted images allow determination of precipitate morphology as described by the histogram.

700AT hardness tester coupled with a Suntec FM-ARS9000 controller. Vickers indentation measurements were made using a 50x objective, a 0.15 mm step size and a 50 g-force load.

Microbeam X-ray diffraction (XRD) of polished cross sections was carried out using a Rigaku D/Max Rapid II micro diffraction system. A parallel X-ray beam collimated to 300 μm diameter was directed onto the specimen from a rotating Cr anode ($\lambda = 2.2910$ Å) operated at 35 kV and 25 mA. The sample was rotated during exposure to minimize texture effects, and diffracted intensities recorded on a large 2D image plate before integration to give powder traces. Full-pattern (Rietveld) refinement was carried out using TOPAS (v5, Bruker AXS) to obtain lattice parameters and estimates of phase fractions.

3. Results

3.1. ShAPE processing

Application of the ShAPE approach with the process parameters shown in Table 2 resulted in the formation of tubes having an outer diameter of 7.5 mm, an inner diameter of 6.0 mm and wall thickness of

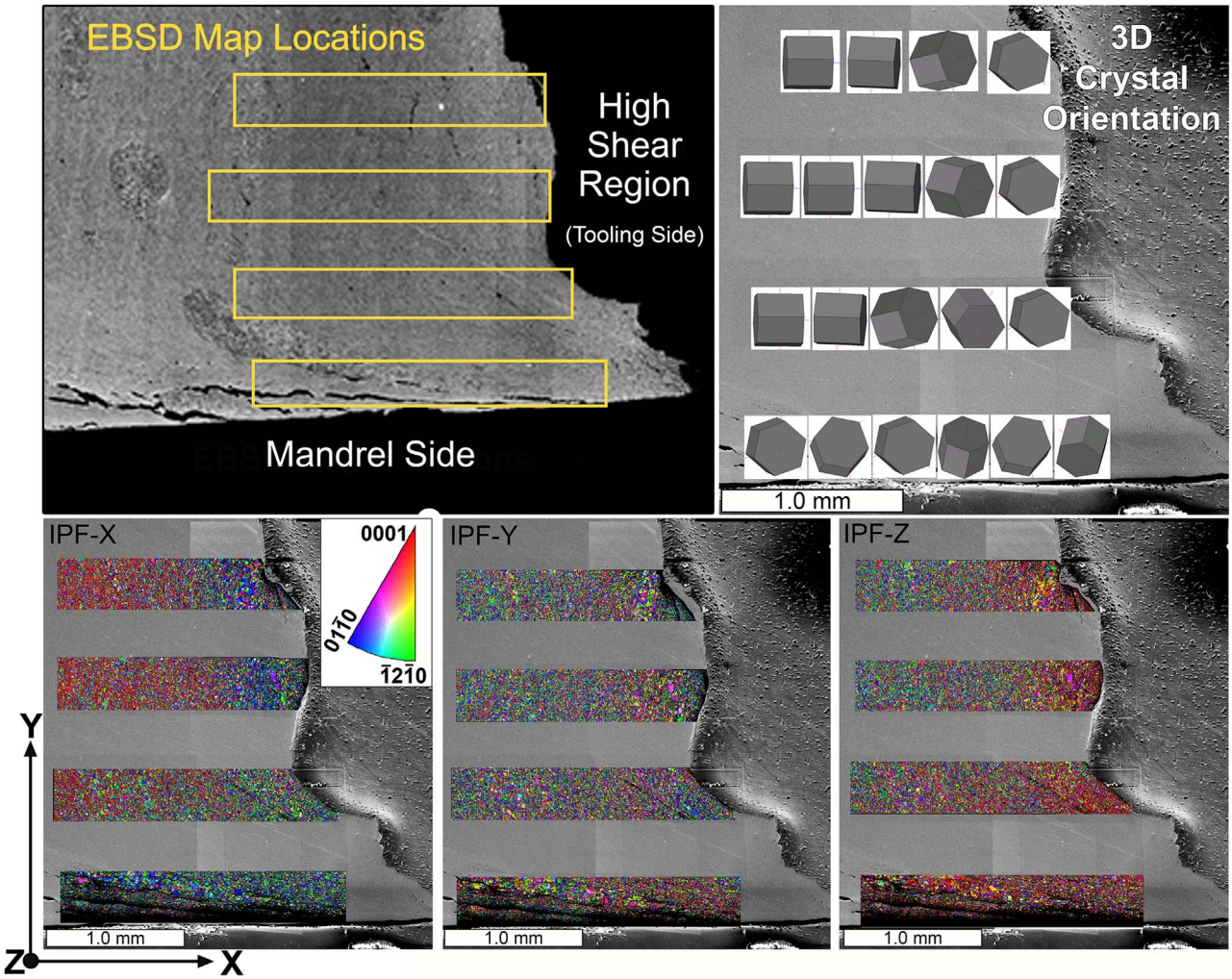

Fig. 11. Large area EBSD inverse pole figure (IPF) mapping illustrates texture transitions present in the compacted puck. The extrusion direction in these images is aligned with the x-axis. Basal texture (red coloring) shifts from alignment in the extrusion direction (IPF-X) deep within the puck to alignment in the out-of-plane direction (IPF-Z) in the high shear region where the compact flake was in contact with the die face. (For interpretation of the references to color in this figure legend, the reader is referred to the web version of this article.)

0.75 mm. Fig. 2 shows the compacted flake material in a puck geometry and a ~2.5 cm long extruded tube. The earing pattern on the right side of the tube is indicative of the first material to be extruded. The tool was extracted upon extrusion at 100 RPM and separation of the tube from the puck occurred as a result of the die extraction step. Residual markings from the single start scroll pattern are observed on the surface of the compacted flake.

Processing parameters and conditions are shown in Fig. 3. During fabrication, the rotating die is plunged downward from a starting position 1.27 mm above the surface of the pre-compacted puck located at 0 mm. Approximately 20 s into the run, the force rapidly builds while the friction between the rotating tool and flake begin to generate heat at the interface. The increase in tool temperature during this time period is observed in Fig. 3b. Also shown is the increase in power (the product of torque and tool speed) that roughly follows the increase in tool force.

The power spike in Fig. 3b at the start of the process is due to inertial resistance associated with increasing the spindle velocity from stationary to 500 RPM and does not contribute to heating since the tool is not in contact with the material at this point. Breakthrough occurs 35 s into the process when the temperature, spindle power and extrusion pressure reach 250 °C, 6 kW and 14.9 MPa respectively. Extrusion pressure and spindle power then fall off to steady-state levels of 8.8 MPa and 3.1 kW respectively while temperature rises to a maximum of 441 °C as the extrusion forms. The intermittent peaks on the power curve are likely due to flashing between the die OD and can ID.

The characterization efforts of this work have been divided into two parts to clearly illustrate the microstructure of the rapidly solidified precursor material as well as that of the compacted and extruded material following ShAPE processing.

3.2. Characterization of AZ91E rapidly solidified flake

The rapidly solidified flake material was characterized using both SEM and TEM. Fig. 4 highlights the precursor microstructure on several different length scales. A container of the as-produced material is shown in Fig. 4a. Fig. 4b and c depict the cross section using an SEM low angle backscatter electron detector and accelerating voltage of 20 kV. Minor changes in contrast show a highly-refined uniform region at one surface of the flake material (likely the first to solidify from contact with the wheel) that transitions at approximately half the flake thickness to a dendritic structure. Higher magnification, 5 kV backscatter imaging reveals the interaction volume under investigation and revealed the presence of a bright and refined second phase, of higher density than the surrounding matrix (Fig. 4d-e).

XRD patterns of the as-synthesized flakes were dominated by peaks corresponding to a hexagonal Mg-rich metal as shown in Fig. 5. The refined lattice parameters of this compound (a = 3.182, c = 5.174 Å) are ca. 0.8% smaller than pure Mg, and correspond to an alloy with ca.

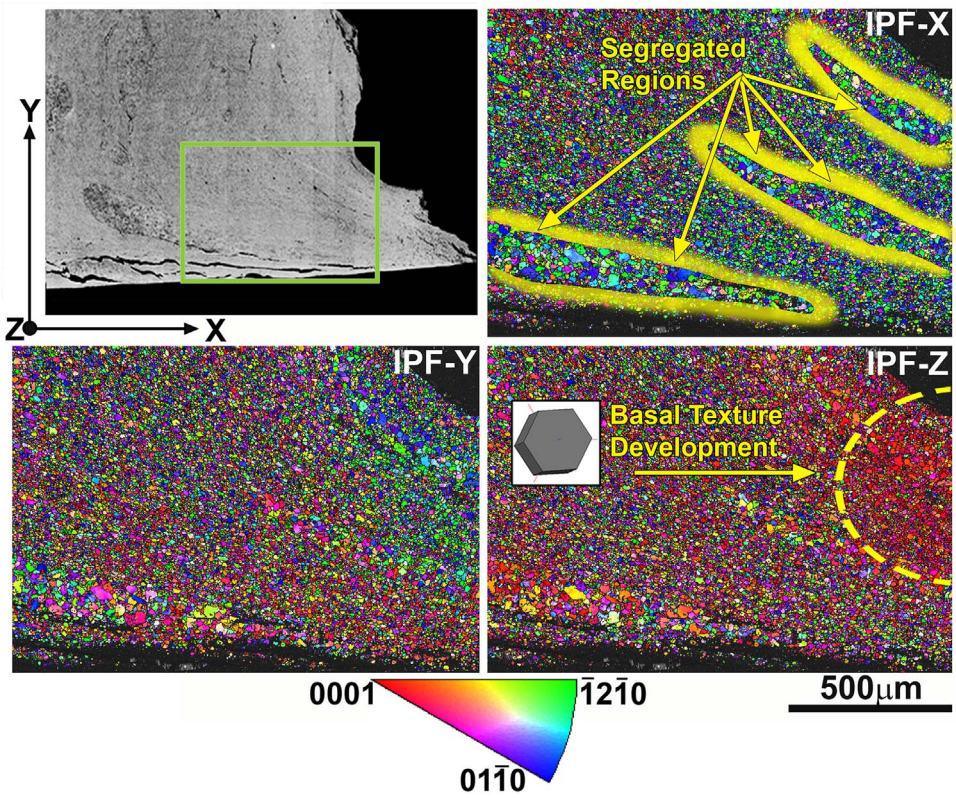

Fig. 12. EBSD of the compacted flake material was performed in the region nearest the extrusion orifice. Compositionally segregated regions coincide with localized grain growth. Strong basal texture development is shown to occur in the region where material flows into the orifice. The x-direction is aligned with the extrusion direction.

6.5 at% Al according to the work published by Ren et al. [38]. This result agrees reasonably well when compared with the ICP-OES compositional analysis reported in Table 1. Weak peaks arising from $Mg_{17}Al_{12}$ are clearly visible in the inset shown in Fig. 5, and quantitation using the Rietveld method indicated that 1.9 ± 0.2 wt% of this compound was present. Non-equilibrium eutectic $Mg_{17}Al_{12}$ has been shown by previous researchers to exist in interdendritic regions of α-Mg dendrites [39]. Several other weak diffraction peaks are also evident which could not be satisfactorily matched with any patterns in the ICDD database, indicating they may be non-equilibrium compositions, or metastable phases formed as a result of rapid solidification processing. This result implies the second phases that were observed in Fig. 4 could correspond to the $Mg_{17}Al_{12}$ phase or a metastable second phase of increased density compared to α-Mg.

The precursor material was further investigated using TEM to evaluate the formation of any highly refined secondary phases that were either metastable or may not have been present in concentrations sufficient to be detected via XRD measurement. A FIB lift-out was prepared from the cross section of a single flake sample. Bright field, as well as STEM high angle annular dark field (HAADF) imaging, indicates the presence of two additional precipitate distributions beyond the $Mg_{17}Al_{12}$ phase identified by microXRD. As seen in the Fig. 6, the top row of images illustrates a representative overview of the specimen structure. A highly refined (< 15 nm) second phase is present, in contrast to larger, blocky precipitates (~75 nm). The bottom row of images compares the scale of the two precipitate types. Contrast in HAADF imaging is proportional to atomic z-number contrast (i.e., heavier elements will appear brighter). These images indicate the smaller precipitates have a higher density than the larger precipitates. And that both are higher density when compared to the surrounding matrix. High resolution TEM performed on the larger precipitates indicated they were crystalline, as illustrated in the Fig. 6 callout. Energy dispersive spectroscopy (EDS) performed on the small precipitates indicated that they are Al and Mn rich while the larger precipitates were found to be rich in Al and Zn.

3.3. Low magnification characterization of AZ91E compacted flake and extruded tube

A cross-section of the compacted flake and extruded tube (extrudate) is shown in Fig. 7. Reflected light images of the divided sample show a homogeneous extrudate cross section, free of porosity. Some regions of diffuse reflection suggesting material inhomogeneity were observed in the compacted flake, and as a result, specimen microstructures were further evaluated in the rectangular areas highlighted in Fig. 7.

SEM (BSE) images were used to identify potential compositional variation in the material. Regions of diffuse reflected light seen in the compacted flake (Fig. 7) were found to correspond with enlarged zones exhibiting localized compositional variation (Fig. 8). These segregated zones were approximately 0.5 mm in thickness and 0.5–2 mm in length. Higher magnification images (Fig. 8 bottom row) reveal the presence of a bright second phase that indicating precipitate formation and growth occurred in the segregated regions at a greater frequency than in the surrounding matrix. The second phase precipitates within these zones of the compacted flake were found to be 2–6 μm in length. ShAPE extrusion was shown to significantly elongate and reduce the overall thickness of segregated zones. One large region is observed in Fig. 8 to be necking down as it approaches the extrusion orifice. BSE imaging of the extrudate shown in Fig. 8 illustrates the typical microstructure, two regions along the tube length are depicted at higher magnification, both revealing a significantly refined and homogeneous second phase distribution. Some small areas of residual segregation are present, but they have been dramatically reduced in size, to ribbon-like zones ~50 μm in width.

Evaluation of the segregated regions from deep within the compacted flake was performed. EBSD of these equiaxed zones showed grain growth when compared to the surrounding matrix (Fig. 9). Grain size in these zones was significantly varied and ranged from 5 μm −115 μm in diameter, several of the large grains were also observed to contain twins.

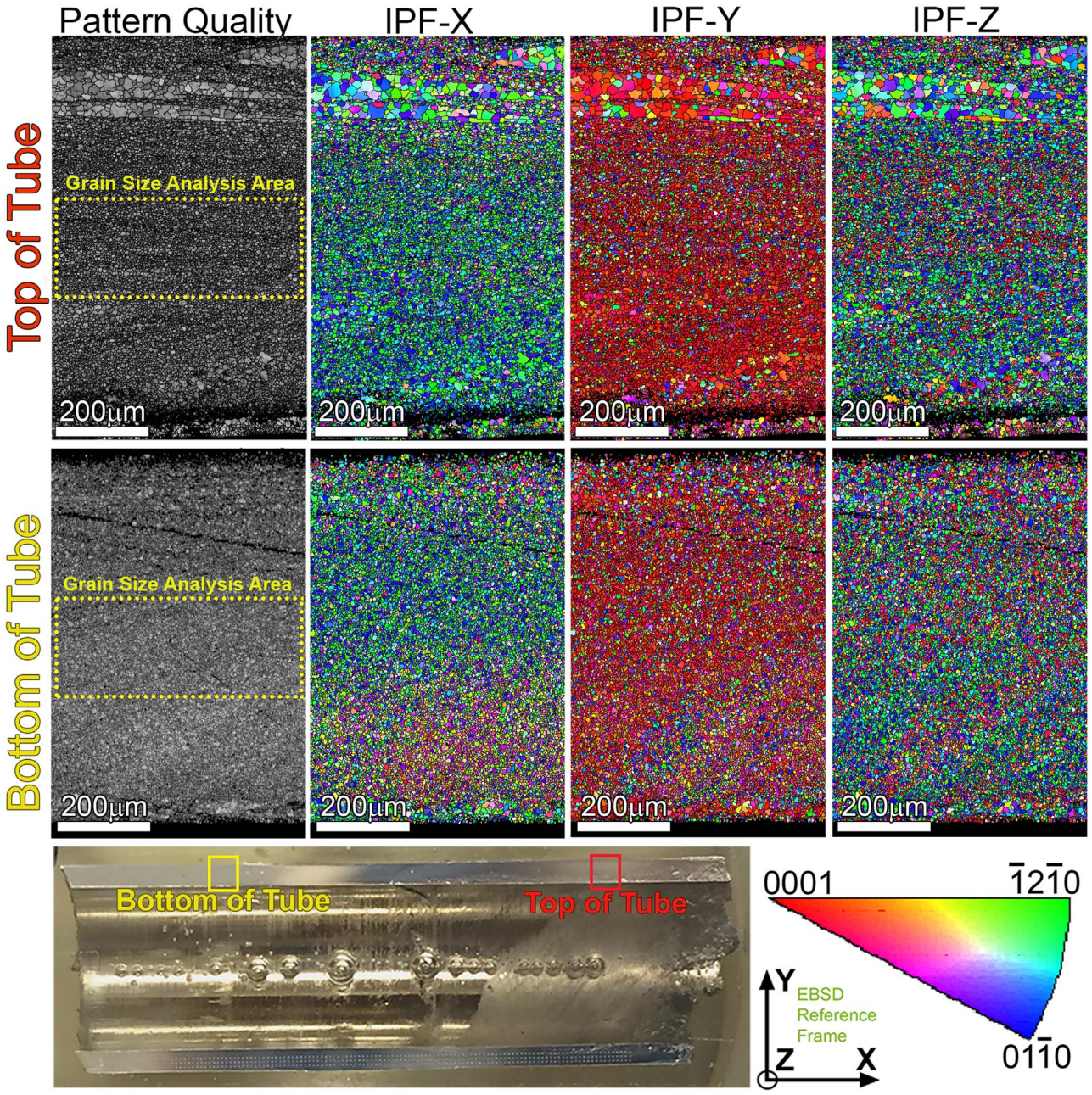

Fig. 13. EBSD mapping was performed through the wall thickness of the extrudate in two regions along the length, approximately 10 mm apart. The texture and grain size evaluated were consistent, with both regions showing a basal texture in the y-direction as oriented in the extrudate diagram. A localized region of larger grain size was seen in the map acquired from the top of the tube.

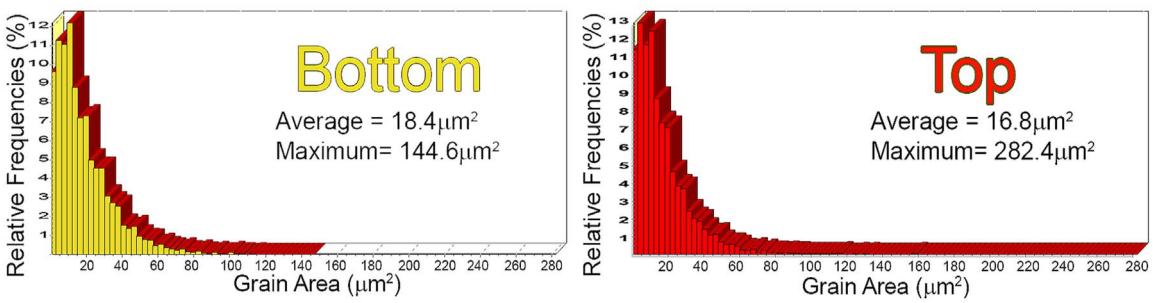

Fig. 14. Histograms of the grain size (area measurement) were generated from the interior 1/3 of the mapped regions shown in Fig. 13. Averages and standard deviations indicate that the typical grain area (excluding the isolated band of larger grains) was consistent throughout the length of the extrudate.

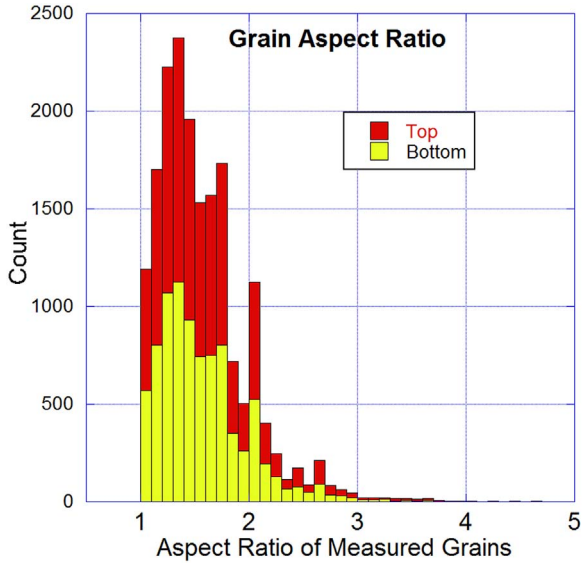

Fig. 15. Histograms of the aspect ratio illustrating grain shape from the regions shown in Fig. 13.

EDS performed on the segregated regions far from the tooling surface of the compacted flake revealed that the precipitated second phases (originally shown in Fig. 8) were Al + Mn or Al + Zn rich phases, indicating growth of the highly-refined phases (initially observed by TEM EDS of the flake precursor) had occurred. EDS mapping was performed on several different length scales and is shown in Fig. 10. Morphology of the precipitates found within the segregated zones is also shown. The contrast-thresholded images in the lower half of Fig. 10 were utilized to evaluate the precipitate size, which ranged from 8 nm to 5 μm along the largest dimension. The equivalent circular diameter (ECD) was calculated which resulted in a mean diameter of 0.69 ± 0.51 μm. A histogram of the precipitate size distribution shows the majority of precipitates within the segregated region have an ECD of less than 2 μm.

To better understand the redistribution of these segregated regions, EBSD was used to evaluate potential grain size and texture development during processing, especially at the tool-billet interface. EBSD of the compacted flake is shown in Figs. 11 and 12. The evolution of basal texture in Fig. 11 illustrates a 90-degree shift in the {0001} orientation from preferential alignment parallel the extrusion direction (at locations far away from the tool surface) to an out-of-plane z-direction basal orientation in the high shear regions where the ShAPE tooling contacts the flake during compaction. It is interesting to note that basal-plane-normal far from the tooling interface was aligned parallel to the applied load. Material interaction with the scroll features at the tool interface (which serves as a conduit for material flow towards the orifice) coupled with the heat generated at the interface results in a 90° shift in basal texture.

Higher magnification EBSD mapping was performed near the extrusion orifice to better illustrate texture and grain size in the high shear region. This additional mapping (Fig. 12) was performed along the tooling side of the compacted flake specimen where the extruded tube was removed from the puck. Segregated regions seen in the BSE images are again shown to coincide with localized grain growth. Also of interest, basal texture aligned in the y-direction has increased when compared to far-from-tooling regions deeper in the puck previously shown in Fig. 11.

EBSD of the extruded tube was mapped through thickness at two locations down the length to evaluate the produced material for homogeneity. Results (Fig. 13) indicate the development of a strong basal texture oriented such that the basal-plane-normal is directed towards the center of the tube. This result indicates a ninety-degree shift in basal orientation about the extrusion axis. The top of the tube (furthest from the extrusion orifice) shows refinement of a segregated region that was present in the compacted flake material. Typical grain areas seen within the segregated zones were measured to have diameters in excess of 100 μm. EBSD mapping at the bottom of the tube, (nearest the extrusion orifice) shows a uniform grain structure with no evidence of residual grain growth.

Overall grain size and shape distributions were generated from the central third of the EBSD maps shown in Fig. 13. Grain size analysis was performed in order to evaluate whether or not a matrix grain size difference was present as a result of varied temperature profiles experienced during fabrication, inherent to the processing technique. The grain size was compared and histograms are plotted in Fig. 14. While the average grain area is very similar (18.4 μm^2 vs. 16.8 μm^2), the bottom of the tube showed a narrower distribution than the top, achieving a maximum grain area approximately half the size seen at the top of the extrudate. The increase in the maximum grain size at the top of the tube indicates some minor grain growth may have occurred. However, the vast majority (~90%) of the grains measured were less than 40 μm^2 in both regions. Grain shape in the two regions was reasonably equiaxed and similar, as shown in (Fig. 15).

Vickers hardness mapping was utilized to evaluate the opposite side (lower half shown in Fig. 13) of the extrusion tube. Testing was performed along three rows, through the thickness of the tube. A diagram of the tested sample is shown in Fig. 16 along with the Vickers hardness plotted as a function of extrudate length. Hardness appears to be relatively consistent with increased deviation seen on the sample ends. Deviation at the ends is likely a result of work hardening during sample removal. The average Vickers hardness was measured to be HV80.3 ± 4.8 using a 50 gf load. Using Tabor's approximation, this estimates a yield strength of 263 MPa [40]. These results are in agreement with similar hardness and yield strength measurements performed on fine grained AZ91 extrusions formed using multipass equal channel angular pressing (ECAP) [41,42].

3.4. High magnification characterization of AZ91E extrusion tube

Because this processing technique was found to result in microstructural evolution (as evidenced by the segregation seen in the compacted puck-Figs. 8 and 9) direct comparison of the RS flake precursor and the final extrudate at a location centered through-thickness at the bottom of the tube (Fig. 17) was performed using EBSD. This was done to determine whether significant grain growth occurred as a result of processing when compared with the initial feedstock material. EBSD

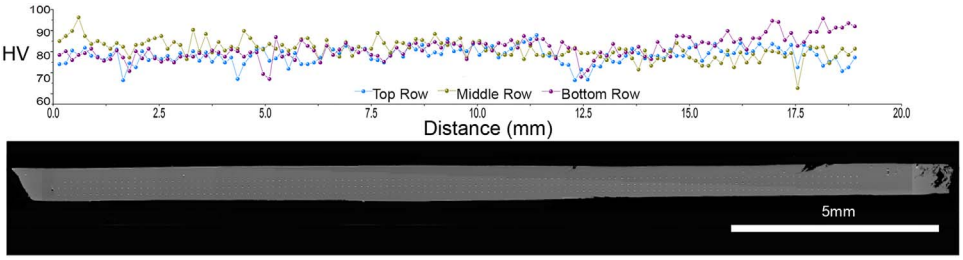

Fig. 16. Vickers hardness measured throughout the length of the extrudate is consistent indicating a microstructural uniformity.

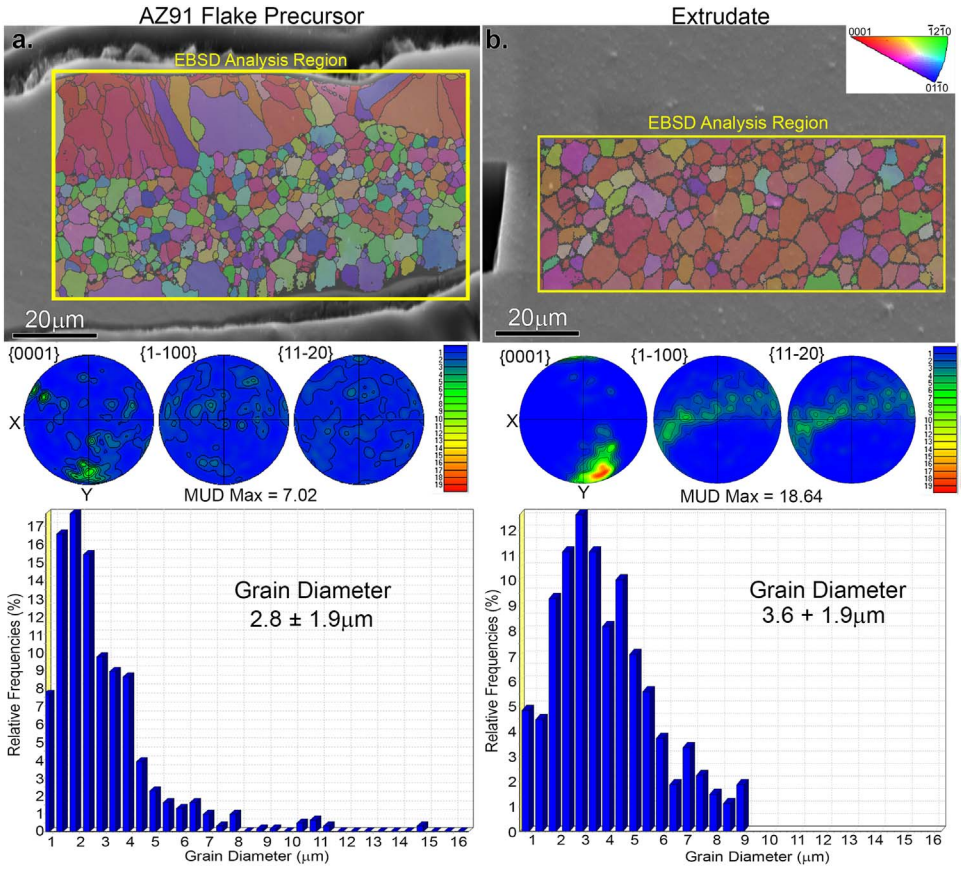

Fig. 17. EBSD orientation maps with inverse pole figure coloring of the flake material (a) and the extrudate (b) are shown and indicate basal texture development occurred during extrusion. The largest grains seen in both specimens indicate considerable grain growth of the precursor material was avoided. (For interpretation of the references to color in this figure legend, the reader is referred to the web version of this article.)

comparison of the flake and extrudate illustrates significant texture development. Multiples of uniform distribution (MUD) maxima were increased from 7.02 to 18.64 as a result of processing.

Grain size seen in the flake material shows a columnar microstructure along one side (15–25 μm on longest dimension) that transitions to an equiaxed structure approximately half way through the thickness. When compared to the consolidated extrudate, the microstructures shown indicate that (while ShAPE processing may result in slight growth of ultra-refined grains seen in the flake as a result of elevated temperature fabrication) simultaneous material homogenization and grain size refinement via high shear processing was able to consolidate the flake material at elevated temperature without substantial grain size increases. Equivalent circular grain diameter of the two specimens indicates ShAPE processing resulted in approximately a two-fold reduction in the largest grain sizes measured.

SEM (BSE) and EDS analyses were also performed on the extrudate at elevated magnification. Fig. 18 shows a region of the sample where second phase particles were found to have segregated along grain boundaries. Two precipitate types were again observed; a random dispersion of larger precipitates with higher atomic number (bright white contrast) and smaller intergranular (IG) precipitates that exhibit less mass contrast (gray). SEM EDS mapping revealed that the larger white particles are aluminum and manganese rich (Fig. 16c,d). The smaller, intergranular precipitates were identified as rich in aluminum and zinc (Fig. 16c,e). This result matches the two refined precipitate distributions initially seen in the TEM EDS results of the precursor flake. It also indicates that the Al + Mn-rich phase (initially < 15 nm in the flake) increased to ~0.6 μm in diameter (measured from Fig. 13) following ShAPE processing. It should be noted that second phase precipitation along grain boundaries was not uniform throughout the extrudate, but was dominant in the banded regions of large grains. Quantitative analysis of the second phase was not performed in the SEM due to the refined size of the particles. For these reasons, a FIB TEM specimen was prepared from the extrudate, near the EBSD analysis region (previously shown in Fig. 17).

TEM analysis performed on the extrudate is shown in Fig. 19. These bright field TEM images illustrate both intergranular (Fig. 19a) and intragranular (Fig. 19b,c) precipitates. As indicated by the SEM analysis, the overall precipitate size in the extrudate was increased when compared with the nanoscale (< 15 nm) precipitates seen in the flake precursor material. TEM EDS line scans were performed on two intragranular particles and indicated a composition of ~30–40 at% Al and approximately 10–15 at% Mn, balanced by Mg, which is compositionally consistent with the SEM results. While composition profiles are not shown in the figure, grain boundary precipitates were found to be composed of ~25–30 at% Al, 1–2.5 at% Zn, balanced by Mg.

Comparison of the consolidated tube to the flake was also performed using microbeam X-ray diffraction, and is shown in Fig. 20. Small changes in the XRD pattern were evident. As a result of consolidation by ShAPE processing, the hexagonal Mg peaks sharpened slightly, which was attributed primarily to a reduction in microstrain based on the 2θ dependence of the line breadths. The lattice parameters of this phase did not change significantly, suggesting little change in composition. A small increase in the fraction of $Mg_{17}Al_{12}$ from ca. 2–3.0 ± 0.2 wt% was observed. Peak heights were reduced for several of the unidentified peaks (2θ ~ 52° and 131°), indicating the high temperature consolidation process may have resulted in slight in-growth of this phase.

4. Discussion

During fabrication of the flake precursor, the high cooling rates inherent to this processing technique resulted in the dissolution of aluminum into the magnesium matrix, forming a solid solution of the alpha phase. XRD indicated very minor amounts (< 2 wt%) of the $Mg_{17}Al_{12}$ phase were present in addition to several other weak diffraction peaks that could not be satisfactorily matched in the ICDD

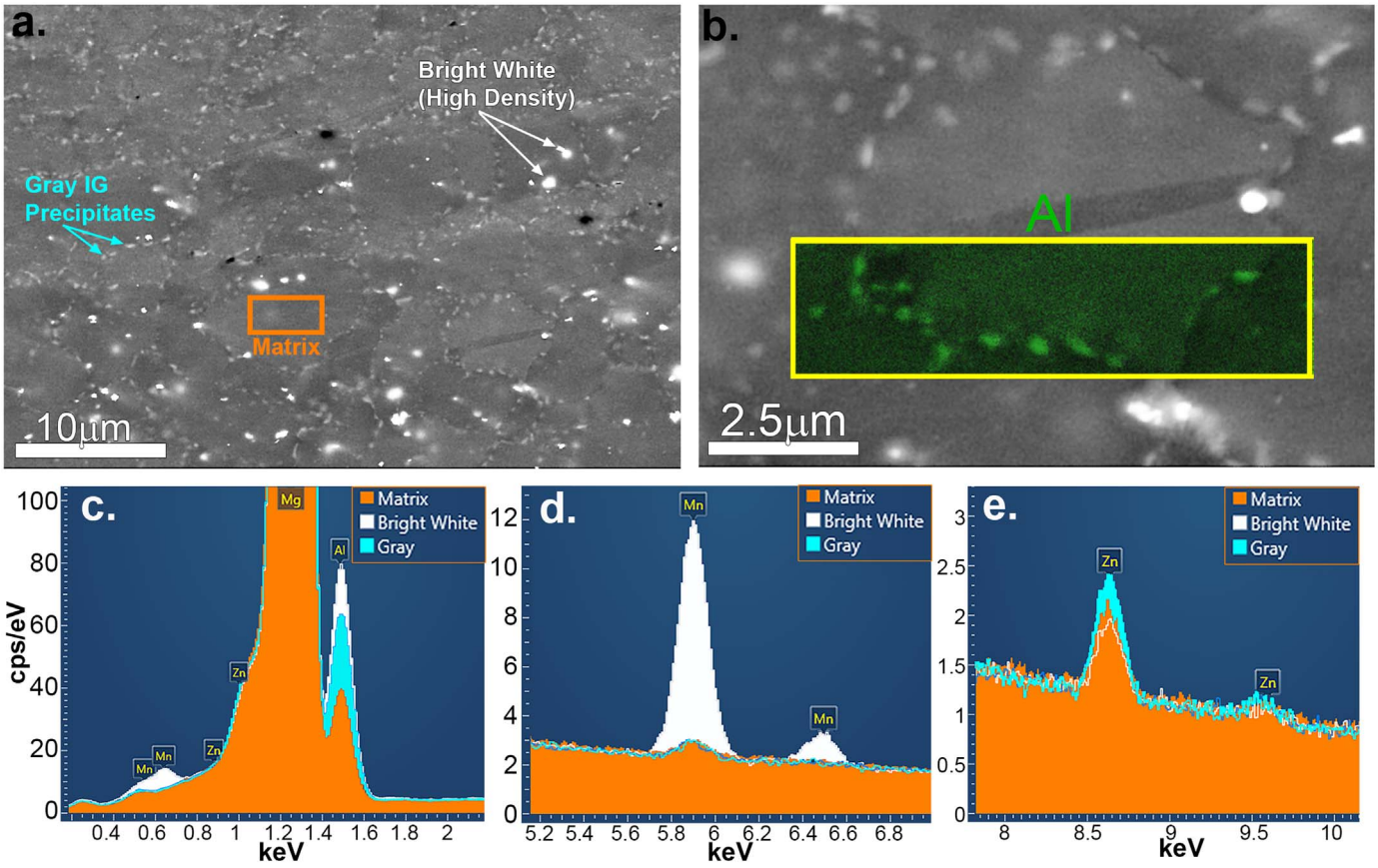

Fig. 18. SEM backscatter images (a, b) of the extrudate cross section show segregation of second phase particles to the grain boundaries in large grained regions. EDS spectral overlays (c-e) show compositional differences in the primary precipitate forming elements (Al, Mn and Zn) with respect to backscatter contrast as indicated in the figure legend. These results are in agreement with compositional information obtained from TEM analysis of the starting flake material.

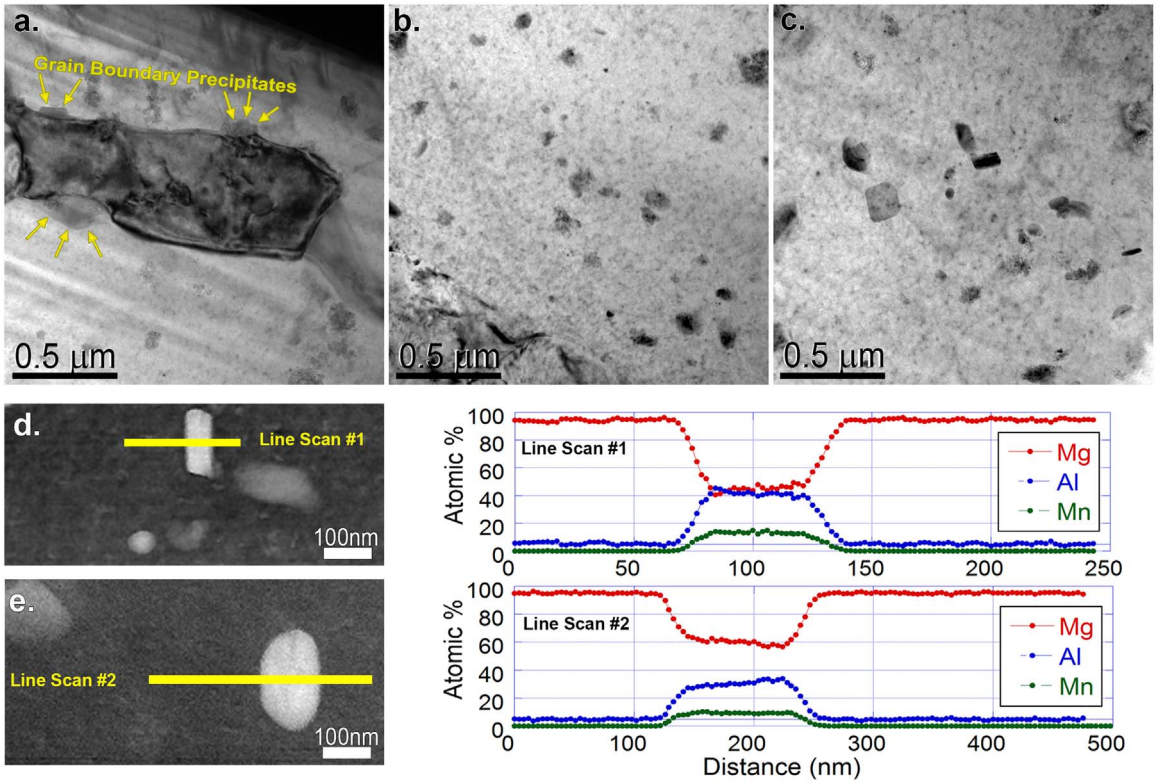

Fig. 19. TEM bright field images of the extruded material show second phase formation on grain boundaries (highlighted in a) as well as two regions showing intragranular precipitate dispersions (b & c). TEM EDS line scans (d and e) show second phase composition.

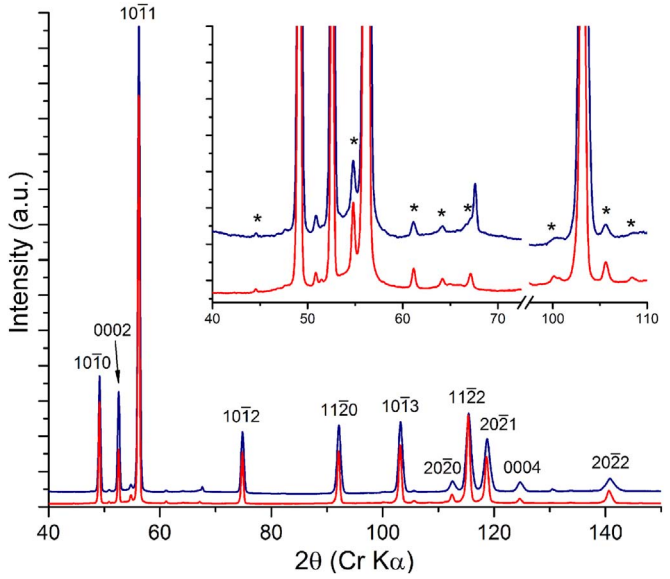

Fig. 20. XRD patterns of flakes (dark blue, upper) and the extrudate (red, lower). Peaks corresponding to hexagonal Mg-rich metal are indexed in the main figure, and those corresponding to $Mg_{17}Al_{12}$ are marked with an asterisk in the inset which has an expanded vertical scale. (For interpretation of the references to color in this figure legend, the reader is referred to the web version of this article.)

database, likely indicative of metastable phase formation as a result of non-equilibrium processing. TEM characterization of the flake further revealed very refined distributions of Mn and Zn rich phases, likely too minor to detect using XRD. Coupled with EDS, TEM investigation revealed the presence of a highly refined Al and Mn-rich (< 15 nm) second phase, in addition to larger, blocky precipitates (~75 nm) that were identified as rich in Al and Zn. Similar observations showing formation of metastable states have been made in related studies [43–45] as well as the formation of non-equilibrium eutectic $Mg_{17}Al_{12}$ [39]. The grains observed in the rapidly solidified flake samples were 16 μm along their largest dimension, as measured using EBSD.

ShAPE processing of the RS flake occurred over a wide tool temperature range (250–441 °C) where the potential for formation of equilibrium precipitates exists. The high temperatures that were reached resulted in formation of distinct zones of localized segregation and grain growth seen within the compacted flake. Melt spinning frequently results in the formation of non-equilibrium or metastable phases due to the very high cooling rates involved. As a result, the segregation observed in the AZ91 precursor material during high temperature compaction was not surprising. The length scale of the segregated zones seen in the compacted flake (1.5 mm × 0.5 mm) is significantly larger than the dimensions of individual flakes, indicating these zones were not the caused by inclusion of atypical flake material, but instead occurred due to thermal instability of the flake precursor. The elevated temperature compaction of the puck material demonstrated an inability to retaining the initial starting microstructure. Precipitates seen in the segregated regions of the compact flake were found to have a mean equivalent circular diameter 0.69 ± 0.51 μm and coincided with localized grain growth. Grain growth of the compacted flake exhibited diameter increases from 16 μm to over 100 μm, as measured along the largest dimension.

Conveniently, the localized zones that exhibited precipitation and grain growth in the compacted puck also enabled assessment of the ShAPE process for its ability to disperse and homogenize segregated, inhomogeneous material. Several of the segregated zones deep within the compacted flake were observed to be relatively equiaxed and circular in cross section. This morphology was shown to elongate and neck down as material approached the extrusion orifice. As a result, the overall size of the segregated zones (observed in the compacted flake) was significantly refined, reducing in thickness from 500 to 750 μm down to thin ribbons of coarser grained material with a total width of < 100 μm, as shown in Figs. 12 and 13.

The key aspect of the compositional information presented in this work is that metastable, or far-from-equilibrium precipitate compositions (initially formed in the precursor flake) can be consolidated despite the high temperature densification during ShAPE processing while limiting extensive precipitation of the $Mg_{17}Al_{12}$ phase. Second phase precipitate compositions that were observed in the precursor flake by TEM were found to be Al + Mn and Al + Zn rich. SEM EDS measurement of the compacted flake showed growth of the Al + Mn phase occurred in the segregated regions. ShAPE processing of the compacted flake homogenized both the precipitate and grain size distributions. Flake chemistries were retained throughout processing and were shown to be present in the extrudate. Despite the high temperature consolidation, quantification by XRD showed concentration of the $Mg_{17}Al_{12}$ phase was only minimally impacted as a result of the high temperature processing, increasing from ~2 wt% to 3 wt%. Grain size was evaluated over the entire length of the tube and extensive grain growth in the extrudate was avoided, average grain size at the center of the extrudate was ~4 μm in diameter with an aspect ratio of ~1.4.

Of specific interest to this study was the ability of this processing approach to impart crystallographic texturing. Results of the microstructural analysis highlight how texture development begins in consolidated flake, transitions in the high shear region and is propagated throughout the length of the extrudate. Consolidated material far from the tooling surface undergoes a hydrostatic stress state while material in the high shear region undergoes simultaneous linear and rotational shear as well as potential temperature gradients. The shifts in basal texture are likely a result of variances in the stress state and active slip systems and will be further investigated in future research efforts. Texture measurements at this point have illustrated the ability of ShAPE processing to impart significant basal texturing to extruded AZ91 material.

5. Summary & conclusion

ShAPE is a novel extrusion technique which was found to offer several significant processing benefits compared to conventional extrusion techniques. Segregated zones present in consolidated material exhibited significant grain size refinement and second phase homogenization due to the high shear involved during processing. The ability to retain second phase particles formed in the initial precursor and impart crystallographic basal texture in the extrusion tube is a unique ability of the approach highlighted in this study. Despite the elevated temperature processing, the presence of the $Mg_{17}Al_{12}$ phase in the final consolidated part remained less than 3 wt%. Vickers hardness measurements of the ShAPE processed tube showed structural uniformity through its entire length and thickness.

Future research efforts on this topic will further characterize and evaluate second phases observed in this study as well as the effect of process parameters such as tool speed, temperature and extrusion rate on final grain size, texture and mechanical properties.

Acknowledgements

The authors would like to recognize U.S. Magnesium LLC for supplying the material used in this study. Financial support for this work was awarded through the MS^3 (Materials Synthesis and Simulation across Scales) Initiative at Pacific Northwest National Laboratory, a multi-program national laboratory operated by Battelle for the U.S. Department of Energy. A portion of this research was performed using EMSL, a DOE Office of Science User Facility sponsored by the Office of Biological and Environmental Research. S.N. Mathaudhu was supported in part by the National Science Foundation under grant no. 1463679. Finally, we would like to thank May-lin Thomas for her ICP-OES

assistance, Stan Pitman for sharing his insight and expertise on melt spinning and high temperature extrusion processing and Eric Nyberg and Jung Pyung Choi for their assistance with RS flake production.

References

[1] E. Ghali, W. Dietzel, K.-U. Kainer, General and localized corrosion of magnesium alloys: a critical review, J. Mater. Eng. Perform. 13 (1) (2004) 7–23.
[2] S.L. Chawla, Materials Selection for Corrosion Control, ASM International, Materials Park, OH, 1993 (ISBN-10: 0-87170-474-9).
[3] M.K. Kulekci, Magnesium and its alloys applications in automotive industry, Int. J. Adv. Manuf. Technol. 39 (9–10) (2007) 851–865.
[4] S.G. Pantelakis, N.D. Alexopoulos, A.N. Chamos, Mechanical performance evaluation of cast magnesium alloys for automative and aeronautical applications, J. Eng. Mater. Technol. 129 (3) (2007) 422–430.
[5] H. Friedrich, S. Schumann, Research for a "new age of magnesium" in the automotive industry, J. Mater. Process. Technol. 117 (3) (2001) 276–281.
[6] E. Aghion, B. Bronfin, D. Eliezer, The role of the magnesium industry in protecting the environment, J. Mater. Process. Technol. 117 (3) (2001) 4.
[7] B.L. Mordike, T. Ebert, Magnesium: properties - applications - potential, Mater. Sci. Eng. 302 (1) (2001) 8.
[8] M. Mokhtarishirazabad, M. Azadi, G. Hossein Farrahi, G. Winter, W. Eichlseder, Improvement of high temperature fatigue lifetime in AZ91 magnesium alloy by heat treatment, Mater. Sci. Eng.: A 588 (2013) 357–365.
[9] S. Avraham, A. Katsman, M. Bamberger, Optimization of composition and heat treatment design of Mg–Sn–Zn alloys via the CALPHAD method, J. Mater. Sci. 46 (21) (2011) 6941–6951.
[10] F. Penghuai, P. Liming, J. Haiyan, D. Wenjiang, Z. Chunquan, Tensile properties of high strength cast Mg alloys at room temperature: a review, China Foundry 11 (4) (2014) 277–286.
[11] Y. Ali, D. Qiu, B. Jiang, F. Pan, M.-X. Zhang, Current research progress in grain refinement of cast magnesium alloys: a review article, J. Alloy. Compd. 619 (2015) 639–651.
[12] L.-N. Zhang, Z.-T. Hou, X. Ye, Z.-B. Xu, X.-L. Bai, P. Shang, The effect of selected alloying element additions on properties of Mg-based alloy as bioimplants: a literature review, Front. Mater. Sci. 7 (3) (2013) 227–236.
[13] D.K. Xu, E.H. Han, Effects of icosahedral phase formation on the microstructure and mechanical improvement of Mg alloys: a review, Progress. Nat. Sci.: Mater. Int. 22 (5) (2012) 364–385.
[14] Y. Guohui, M. Tan, Z. Liu, G. Quan, International Conference on Future Energy, Environment, and Materials Effects of Hot Extrusion and Heat Treatment on Mechanical Properties and Microstructures of AZ91 Magnesium Alloy, Energy Procedia 16, 2012, pp. 457-460.
[15] I.J. Polmear, Magnesium Alloys, Light Alloys - From Traditional Alloys to Nanocrystals, Elsevier, Burlington, MA, 2006, pp. 237–298 (ISBN: 0 7506 6371 5).
[16] J.-F. Nie, Precipitation and hardening in magnesium alloys, Metall. Mater. Trans. A 43 (11) (2012) 3891–3939.
[17] Z. Zhang, H. Yu, G. Chen, H. Yu, C. Xu, Correlation between microstructure and tensile properties in powder metallurgy AZ91 alloys, Mater. Lett. 65 (17–18) (2011) 2686–2689.
[18] J.F. Nie, Effects of precipitate shape and orientation on dispersion strengthening in magnesium alloys, Scr. Mater. 48 (8) (2003) 1009–1015.
[19] A. Russell, K.L. Lee, Structure-Property Relations in Nonferrous Metals, Wiley, Hoboken, NJ, 2005 (ISBN-10: 0-471-64952-X).
[20] K.M. Asl, Improving the Properties of Magnesium Alloys for High Temperature Applications, INTECH Open Access Publisher, 2011 (ISBN: 9533075201).
[21] Y. Li, Y. Chen, H. Cui, B. Xiong, J. Zhang, Microstructure and mechanical properties of spray-formed AZ91 magnesium alloy, Mater. Charact. 60 (3) (2009) 240–245.
[22] Z.Z. Zhou, W. Yang, S.H. Chen, H. Yu, Z.F. Xu, Combined effect of non-equilibrium solidification and thermal annealing on microstructure evolution and hardness behavior of AZ91 magnesium alloy, Phys. B: Condens. Matter 443 (2014) 35–42.
[23] F.H. Froes, Y.-W. Kim, S. Krishnamurthy, Rapid solidification of lightweight metal alloys, Mater. Sci. Eng.: A 117 (0) (1989) 19–32.
[24] B. Cantor, Novel Nanocrystalline Alloys and Magnetic Nanomaterials, CRC Press, London, UK, 2004 (ISBN: 0 7503 1002 2).
[25] N.R. Overman, S.N. Mathaudhu, J.P. Choi, T.J. Roosendaal, S. Pitman, Microstructure and mechanical properties of a novel rapidly solidified, high-temperature Al-alloy, Mater. Charact. 112 (2016) 142–148.
[26] J. Cai, G.C. Ma, Z. Liu, H.F. Zhang, Z.Q. Hu, Influence of rapid solidification on the microstructure of AZ91HP alloy, J. Alloy. Compd. 422 (1–2) (2006) 92–96.
[27] H.-t. Teng, T.-j. Li, X.-l. Zhang, Z.-t. Zhang, Influence of sub-rapid solidification on microstructure and mechanical properties of AZ61A magnesium alloy, Trans. Nonferrous Met. Soc. China 18 (2008) s86–s90.
[28] X. Jiang, S.A. Whalen, J.T. Darsell, S.N. Mathaudhu, N.R. Overman, Friction consolidation of gas-atomized FeSi powders for soft magnetic applications, Mater. Charact. 123 (2017) 166–172.
[29] S. Whalen, S. Jana, D. Catalini, N. Overman, J. Sharp, Friction consolidation processing of n-Type bismuth-telluride thermoelectric material, J. Electron. Mater. 45 (7) (2016) 3390–3399.
[30] V.V. Joshi, S. Jana, D. Li, H. Garmestani, E. Nyberg, C. Lavender, High Shear Deformation to Produce High Strength and Energy Absorption in Mg Alloys, Magnesium Technology, 2014 John Wiley & Sons, Inc, Cham, CH, 2014, pp. 83–88 (ISBN 978-3-319-52391-0).
[31] X. Li, W. Tang, A.P. Reynolds, Material Flow and Texture in Friction Extruded Wire, Friction Stir Welding and Processing VII, John Wiley & Sons, Inc, Switzerland, 2013, pp. 339–347 (ISBN 978-3-319-48582-9).
[32] R.A. Behnagh, R. Mahdavinejad, A. Yavari, M. Abdollahi, M. Narvan, Production of wire From AA7277 aluminum chips via friction-stir extrusion (FSE), Metall. Mater. Trans. B 45 (4) (2014) 1484–1489.
[33] R.A. Behnagh, N. Shen, M.A. Ansari, M. Narvan, M.K.B. Givi, H. Ding, Experimental analysis and microstructure modeling of friction stir extrusion of magnesium chips, J. Manuf. Sci. Eng. 138 (4) (2016) 041008.
[34] G. Buffa, D. Campanella, L. Fratini, F. Micari, AZ31 magnesium alloy recycling through friction stir extrusion process, Int. J. Mater. Form. (2015) 1–6.
[35] H. Zhang, X. Zhao, X. Deng, M.A. Sutton, A.P. Reynolds, S.R. McNeill, X. Ke, Investigation of material flow during friction extrusion process, Int. J. Mech. Sci. 85 (2014) 130–141.
[36] F. Abu-Farha, A preliminary study on the feasibility of friction stir back extrusion, Scr. Mater. 66 (9) (2012) 615–618.
[37] M. Sarkari Khorrami, M. Movahedi, Microstructure evolutions and mechanical properties of tubular aluminum produced by friction stir back extrusion, Mater. Des. 65 (1980–2015) (2015) 74–79.
[38] Y.P. Ren, G.W. Qin, W.L. Pei, H.D. Zhao, Y. Guo, H.X. Li, M. Jiang, S.M. Hao, Isothermal section of the Mg–Al–Mn ternary system at 400 °C, J. Alloy. Compd. 479 (1–2) (2009) 237–241.
[39] S.C.S.T. Sakamoto, T. Matsumoto, K. Nakai, S. Kobayashi, S. Matsuda, W. Tang, G.F. Tu, Microstructure and mechanical property in Cast AZ91 magnesium alloy with Y addition, Mater. Sci. Forum (2014) 472–477.
[40] D. Tabor, The Hardness of Metals, Clarendon Press, Oxford, 1951.
[41] Y. Yuan, A. Ma, J. Jiang, F. Lu, W. Jian, D. Song, Y.T. Zhu, Optimizing the strength and ductility of AZ91 Mg alloy by ECAP and subsequent aging, Mater. Sci. Eng.: A 588 (2013) 329–334.
[42] B. Chen, D.-L. Lin, L. Jin, X.-Q. Zeng, C. Lu, Equal-channel angular pressing of magnesium alloy AZ91 and its effects on microstructure and mechanical properties, materials Science and engineering: a, 483 (2008) 113–116.
[43] D.M. Herlach, B. Feuerbacher, Non-equilibrium solidification of undercooled metallic melts, Adv. Space Res. 11 (7) (1991) 255–262.
[44] J. Burššík, M. Svoboda, A HREM and analytical stem study of precipitates in anAZ91 magnesium alloy, Microchim. Acta 139 (1) (2002) 39–42.
[45] A. Inoue, H. Kimura, K. Amiya, Developments of aluminum-and magnesium-based nanophase high-strength alloys by use of melt quenching-induced metastable phase: bulk amorphous, nano-crystalline and nano-quasicrystalline alloys IV, Mater. Trans.-JIM 43 (8) (2002) 2006–2016.